Numerical study of the effects of particle shape and polydispersity on permeability

Xavier Garcia,[1,*] Lateef T. Akanji,[1,†] Martin J. Blunt,[1,‡] Stephan K. Matthai,[2,§] and John Paul Latham[1,‖]
[1]*Department of Earth Science and Engineering, Imperial College London, SW72AZ London, United Kingdom*
[2]*School of Petroleum Engineering, Montanuniversität, Max-Tendler-Strasse, A-8700, Leoben, Austria*
(Received 11 May 2009; published 26 August 2009)

We study through numerical simulations the dependence of the hydraulic permeability of granular materials on the particle shape and the grain size distribution. Several models of sand are constructed by simulating the settling under gravity of the grains; the friction coefficient is varied to construct packs of different porosity. The size distribution and shapes of the grains mimic real sands. Fluid flow is simulated in the resulting packs using a finite element method and the permeability of the packs is successfully compared with available experimental data. Packs of nonspherical particles are less permeable than sphere packs of the same porosity. Our results indicate that the details of grain shape and size distribution have only a small effect on the permeabilty of the systems studied.

DOI: 10.1103/PhysRevE.80.021304 PACS number(s): 45.70.−n, 91.60.Np, 47.56.+r, 47.11.−j

I. INTRODUCTION

The prediction of physical properties of porous materials such as the electric conductivity, elastic properties, or the hydraulic permeability κ is long-standing problem with many applications in science and engineering. In the oil industry, for instance, κ determines the rate at which hydrocarbon can be extracted from a reservoir.

Following previous work [1–4], κ can be expressed as

$$\frac{\kappa}{l_c^2} = \gamma(\phi)\kappa_o(x_1,x_2,\ldots), \tag{1}$$

where l_c is a characteristic length scale of the medium, defined as the harmonic mean grain diameter, the specific surface of the porous medium or an equivalent grain size [1,5–8]. The term $\gamma(\phi)$ denotes the dependency of the permeability on the porosity and κ_o is a geometric parameter, which depends on the variables x_i related to the details of how the voids and solids are distributed, i.e., connectivity, tortuosity, and shape/size of grains, throats and pores among others [6,7,9–18].

The complexity of the void space hinders closed analytical solutions to predict permeability. To date, direct simulation of flow has used models of porous media derived from sphere packs with various modifications to predict permeability.

Bryant *et al.* [19] modeled a sandstone by a system of monosized spheres and computed the flow using a pore-network representation of the void space. The results reproduced the permeability-porosity trend measured for Fontainbleu sandstone. The network model was also used to compute multiphase flow [20]. Bakke and Øren [21] took a similar approach to model different sandstones. To account for the effects of the aspherical grain shape, Schwartz *et al.* [22] first constructed packs of spheres. Then, the center of the spheres was kept fixed while their shape was deformed into ellipses. The permeability was then estimated by effective medium approximations. It was shown that the particle shape has a strong influence on the permeability anisotropy. In a later paper Piloti [23] also deformed the surface of the spheres in a pack to model the real aspherical grains in a sandstone. An extension of the work on spheres was presented by Coelho *et al.* [8] who directly simulated the settling of monosized aspherical particles (ellipsoids, parallelepipeds). The authors found that in the high porosity range $40\% < \phi < 80\%$ the studied packs had *similar* hydraulic properties at a given porosity regardless of the shape of the particles used in the numerical models. Similar conclusions were recently obtained by Lehmann *et al.* [24] after studying packs of overlapping ellipsoids constructed by a stochastic method. The authors concluded that the porosity and surface area dominate the permeability.

Spatial correlations on the void space result from a dynamic process not captured by stochastic methods [25]. In addition, grains are polydisperse in size and shape and only in idealized cases are the shape of the particles are ellipsoids, spheres, or other simple geometric forms. In this paper we construct and compare several granular packs by simulation of settling under gravity. Hence, the spatial correlations arise from a realistic dynamic process. Following [26], we extend previous numerical techniques used for spheres to model grains of different shape found in natural sands.

Five sets of samples are constructed for which the permeability is computed by direct flow simulation on the pore space. The effect of particle shape and polydispersity are studied. The sets labeled *A*, *B*, and *C* share a Gaussian grain size distribution that models a well sorted sand such as Ottawa sand (see [27]). For the set *A*,*B*, we use irregular particles differing in the details of the particle shape. The general description of the particles resemble the form of rounded and well worked grains as found in sands such as Ottawa sand [27,28] or the rounded/compact quartz sand grains studied by Miller *et al.* [29]. For the set *C* we kept the same Gaussian size distribution but all the particles are perfect spheres.

*xgarcia@imperial.ac.uk
†l.akanji06@imperial.ac.uk
‡m.blunt@imperial.ac.uk
§stephan.matthai@unileoben.ac.at
‖j.p.latham@imperial.ac.uk

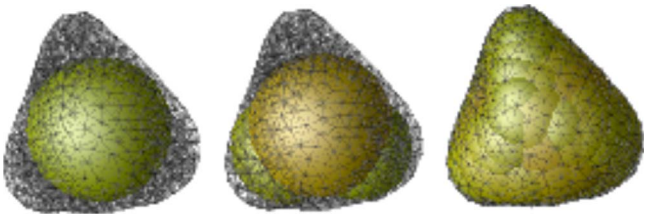

FIG. 1. (Color online) Irregular particles are constructed by sequentially adding spheres to the volume enclosed by a volumetric mesh. From left to right in the figure, an irregular particle is constructed by sequentially adding 1, 3, and ≈30 spheres. The mesh itself was obtained from a shape library [30] or publicly available data from sand grains [31,32].

The effect of polydispersity is studied by comparing the aforementioned models with two other set of samples, labeled D and E. The set D comprises monosized spheres. For the set E we chose similar particles to the sets A,B but the size of the grains is assigned according with a broader size distribution. In this case we took as a guide the experimental sieve analysis as reported for the sand $F110$ in [27]. In comparison with the previous packs of polydisperse spheres and irregular particles, the samples in D,E mainly differ in the degree of heterogeneity. Finally, we compare our results with experimental permeability-porosity correlations reported previously in the literature.

II. METHODOLOGY

A. Modeling aspherical particles

To construct the irregular particles we follow [26]. The shape of the particle is defined by a surface mesh obtained via scanning. A model particle is then constructed by sequentially adding spheres to the volume enclosed by the mesh (see Fig. 1). As more spheres are added, the enclosing surface of the cluster approximates the surface of the real particle represented in the original mesh. Although this method has been used before to model simple irregular particles [33–37], little effort has been made in modeling realistic shapes [34,37] such as that one in Fig. 1.

Here, we construct the sand models using the shapes shown in Fig. 2. For the shapes $G1-G4$ the mesh was obtained from a shape library [30] of real particles scanned in our facilities. The particle $G1$, for instance, is a semispherical particle constructed from a real grain. The particle $G2$ corresponds to an elongated gravel particle. The particles $G3$, $G4$ are pebbles from different sources. The particle $G5$ was constructed by arbitrarily clustering spheres to model an additional elongated particle not available in our database. For the purpose of comparison, Fig. 2 also shows a perfect sphere as was used in previous work to model real grains. In principle, more irregular shapes can also be constructed but the number of spheres per grain raises sharply. Consequently, very irregular grains or pointed particles such as rock fragments or crushed sands are not efficiently modeled (see [26]) with the proposed methods.

TABLE I. Coarse shape descriptors for the particles in the Fig. 2. ψ: Wadell's sphericity. α: aspect ratio computed following [29]. S_v: compactness computed as S_v=surface/(volume)$^{2/3}$ [29].

Particle	ψ	α	S_v
$G1$	0.93	1.28	5.16
$G2$	0.91	2.18	5.25
$G3$	0.96	1.33	5.10
$G4$	0.94	1.35	5.15
$G5$	0.93	1.52	5.18
$S1$	1	1	4.84

Among the shapes that can be modeled, those in Fig. 2 were selected based on visual inspection of two-dimensional (2D) cuts of CT scans of and microphotographs for Ottawa sand in [27,28]. Most of the grains are well rounded and semispherical such as the case of the grains $G1$, $G3$, and $G5$ in Fig. 2. Quantitative measurements at grain scale performed by Miller *et al.* [29] in a different clean sand also served as a guide. The authors reported typical aspect ratios in the range $\alpha=1.2-1.5$ and some elongated particles of aspect ratio up to $\alpha=2.3$. Typical sphericities were in the range $\psi\approx 0.88-0.97$. The compactness parameter S_v =surface/(volume)$^{2/3}$ was $S_v\approx 5.2$ regardless of the particle size. Other authors reported similar values for reference sands with well worked grains [38]. As Table I shows, the shape descriptors for the irregular shapes selected here are in the range of the values reported by Miller *et al.* [29].

B. Shape and size selection

Five sets of samples are constructed with the particles in Fig. 2. Each set, comprises several samples corresponding to different realizations in which the particle shape and/or heterogeneity are fixed. From set to set, the details of grain shape and the size distributions are varied.

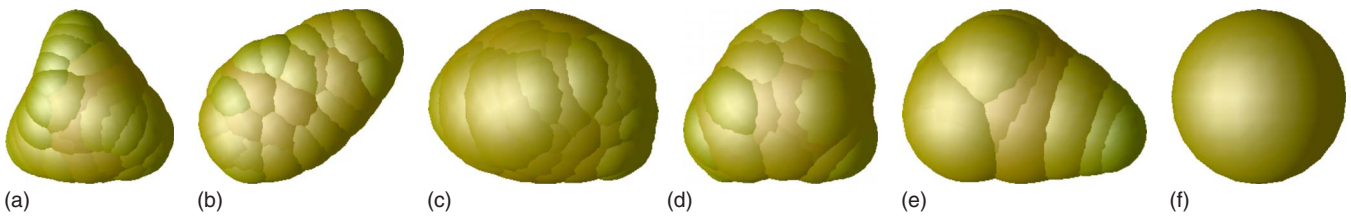

FIG. 2. (Color online) Examples of the model particles constructed by overlapping spheres. Particles $G1-G4$, model real particles scanned in [30]. The particle $G5$ was constructed by arbitrarily clustering spheres to construct a pointed particle. A perfect sphere ($S1$) is also shown for comparison.

TABLE II. Size distribution and grain shape distribution for the five samples in Fig. 4 used in the simulations.

Sample	Size	*G*1	*G*2	*G*3	*G*4	*G*5	*S*1
A	Gaussian	0.28	0.32	0.3		0.1	
B	Gaussian	0.18	0.66	0.16			
C	Gaussian						1.0
D	Monosized						1.0
E	Bimodal		0.4		0.25	0.35	

1. Model A

Model *A* mimics a relatively clean and homogeneous pack such as Ottawa sand. Table II shows the fraction of each grain shape used. The sample was constructed with a large fraction of the rounded and low aspect-ratio grains $G1, G3, G4$, but we selected preferentially the shapes $G1$ and $G3$ because they are visually closer to the pictures of grains of Ottawa sand presented in [28]. A smaller fraction of the grains were given the shape $G2$.

We adopted the criterion in which the size D_g of a grain is defined by the diameter of the sphere that has the same volume as the grain. This size was assigned according to a Gaussian function relating the grain diameter D_g with the volume fraction $V(D_g)$ of the grains of that size (as in sieve analysis). Figure 3 shows the size distribution used, normalized by its maximum height. Here, the distribution is centered in $D_g=520$ μm, to correspond the arithmetic mean grain size obtained from the 2*D* cuts of Ottawa *F*42 in [27]. The width of the distribution was also estimated from the sieve data in [27]. To model such distribution, each grain in the sample was given one of six possible sizes $d_1, d_2, \ldots, d_6$ equispaced between 320 and 670 μm (see Fig. 3) in such a way that the final volume fraction $V(D_g)$ of grains of size D_g in the sample is approximately given by the envelope of the Gaussian distribution as seen in Fig. 3. We randomly assigned shapes according to the ratios in Table II.

2. Models B and C

Both sets have the same size distribution as set *A*, but the details of the grain shape are different (see Table II). In the model *B*, we assigned the elongated shape $G2$ to a greater fraction of the grains (≈66%). The remaining fraction of the grains were given the shapes $G1$ and $G3$ in similar proportions. In the model *C* all the particles are spheres, see Table II.

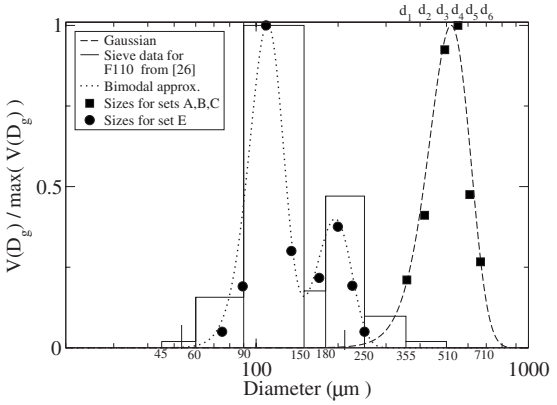

FIG. 3. Volume fraction $V(D_g)$ of the grains of diameter D_g relative to the maximum volume fraction for different packs.

3. Model D

The set *D* has spheres, all of diameter $D_g=520$ μm. In comparison with the rest of the models, this one represents an extremely idealized case of homogeneity and simplicity in the grain shape. These samples can be directly compared with those in model *C*, to address the effect of polydispersity on the hydraulic properties.

4. Model E

In the case of set *E* we aimed to model a more heterogeneous sand. As a guide, we took the experimental sieve data presented in [27] for the sample *F*110. These data were approximated with a continuous distribution as shown in Fig. 3. Following the same procedure described before, eight sizes were sampled from the function and the size of the grains assigned accordingly. The shape of each grain was chosen from the irregular shapes $G2$, $G4$, and $G5$ (see Table II). Figure 4 shows pictures of packings of all the models, illustrating the differences in grain size and shape.

C. Simulation of settling

1. Dynamic model

Once the size and shape of the grains in each model is set, the packs are constructed by simulation of the settling under gravity of the grains. The method used is the discrete element method (DEM) pioneered by Cundall and Stark [39] that has been largely used to model particulate systems (see for instance [40] among others [41–43]).

Contrary to continuum methods such as finite difference or finite elements (FEs), in DEM simulations the particles are treated as individual objects. The dynamical parameters such as the positions and velocities of the particles are monitored during the course of the simulation and updated according to the laws of classical mechanics. Rotations are described by the Euler equation and translations by Newton's second law.

$$F_i = \sum_{j \neq i} F_{ij} + F_{ext} = m_i \frac{d^2 r_i}{dt^2}, \tag{2}$$

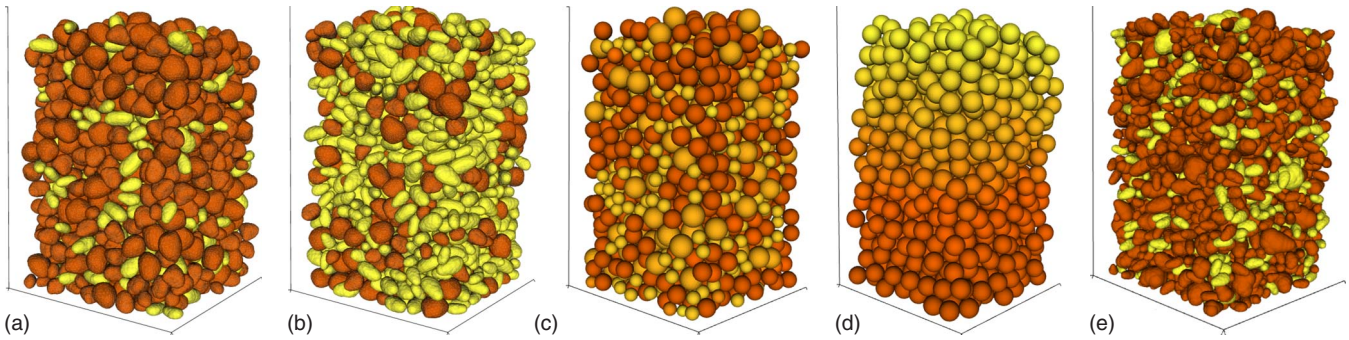

FIG. 4. (Color online) *A*: model *A* of a relatively homogeneous sand with semispherical grains. *B*: model *B*, as the previous model but a large number of grains were replaced by elongated grains (light colors). *C*: model *C*, spheres with the same size distribution as in *A*,*B*. *D*: single size spheres. *E*: more heterogeneous sample constructed with a mixture of irregular shapes.

$$\tau_i = \sum_{j \neq i} (r_{cm} - r_c) \times F_{ij} = \frac{d}{dt}(\mathbf{I} \cdot \omega_i). \tag{3}$$

The term F_i in Eq. (2) represents the total force acting on the particle i. m_i is the particle mass, τ_i is the torque due to the force acting on the contact point r_c and r_{cm} is the center of mass of the particle (see Fig. 5). The term $\mathbf{I}$ stands for the inertia tensor for each particle (as a rigid body) and ω_i is the angular velocity. F_{ext} is the external force acting on the particle system. In our case, F_{ext} is the weight of the particle. The term F_{ij} denotes the interaction force between the particle i and the other j particles. This interaction occurs whenever the spheres pertaining to different clusters overlap. The force is decomposed in one component acting along the normal to the contact, F_{ij}^n, and a tangential component F_{ij}^s (see Fig. 5).

$$\mathbf{F}_{ij} = \mathbf{F}^n + \mathbf{F}^s, \tag{4}$$

$$\mathbf{F}_{ij}^n = \kappa_n (\delta_n R_f)^{1/2} (\delta_n - \gamma_n \dot{\delta}_n) \hat{n}. \tag{5}$$

The normal force F^n is calculated according with Eq. (5) following the classical Hertz model [44,45], where κ_n is a material dependent stiffness constant, chosen to assure a minimum overlap between the particles and reasonable simulation times (see for instance [46]). The term γ_n is a damping coefficient, δ_n denotes the overlapping between contacting spheres and $(\delta_n R_f)^{1/2}$ represents the radius of the contact area according with the Hertz model. For the particles radius R_i and Rj, $R_f = [R_i R_j / (R_i + R_j)]$. The direction of the normal is given by $\hat{n} = (r_i - r_j)/|(r_i - r_j)|$ where r_i, r_j denote the global positions of the two spheres in contact.

$$\mathbf{F}^s = \min\{[\kappa_s (\delta_n R_f)^{1/2} (\delta_s - \gamma_s \dot{\delta}_s), \mu |F_n|]\ \hat{s} \tag{6}$$

The tangential part of the interaction given in Eq. (6) models the stick-slip behavior of the surfaces in contact. The coefficient $\kappa_s = (2/7)\kappa_n$ is the tangential stiffness, γ_s is a damping constant and μ is the Coulomb friction coefficient.

2. Packing algorithm

The construction of the packs starts with an empty box of dimensions $8 \times 8 \times 12$ in units of the mean particle diameter. Periodic boundary conditions are used in the plane xy. As shown in Fig. 6(A), a subset of N grains is then placed above the bottom wall without contacting each other. The newly introduced grains are then allowed to fall under gravity and interact with the bottom wall and other grains. When the kinetic energy of the system reaches a negligible value and every grain contacts either the wall or another grain, a new bath of grains enters in the box above those previously deposited [Fig. 6(B)]. This process repeats itself until the initial box is filled [Fig. 6(C)]. Figure 4 shows examples of the packs constructed with different particle shapes and grain size heterogeneity. Each sample has about 2.5×10^3 grains.

Contrary to some previous work [8,21,47] we do not freeze particles at any stage. Hence, each new subset of particles entering the box interacts with previously deposited particles, allowing for future relocation of already settled grains. This benefits the creation of denser packs and one would expect it to mimic closer what would happen in a real situation.

D. Pore-space CAD model and boundary conditions

An inner core (subvolume) far from the boundaries of the original packs generated in Sec. II C is extracted to avoid boundary effects such as distortions in the solid skeleton or zones of abnormal porosity. The dimensions are in the range 5–6 and 6–7 times the mean grain diameter in the horizontal and vertical directions respectively. This subvolume exceeds the minimum representative volume (REV) reported for sphere packs in [48] and is close to the REV reported heterogeneous sands/sandstones [49–52].

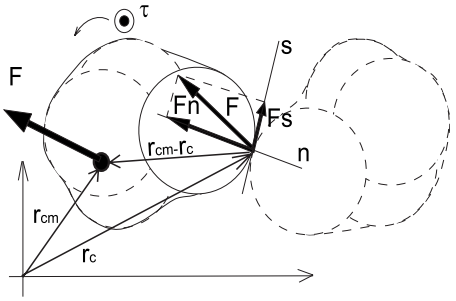

FIG. 5. Interaction between two clusters of spheres (see text).

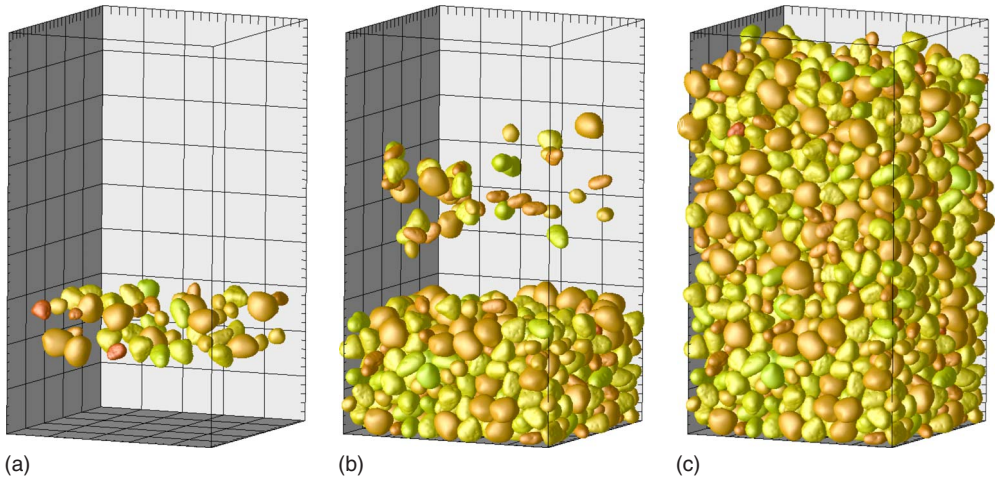

FIG. 6. (Color online) The grains fall under gravity and are allowed to rearrange during the whole simulation. Periodic boundary conditions are used in the plane *xy* to minimize wall effects.

The grains or parts thereof that are not contained in the subvolume are discarded. The resulting packs consisting of ≈300 to 400 grains are then differentiated into two domains: *Grains* and *Pores*, in a computer aided design (CAD) geometrical package. This is accomplished with nonuniform rational *B*-spline (NURBS) curves and surfaces [53].

By modeling the grain packs with NURBS, we are able to capture them with a tolerance-based level of detail, independent of scale allowing a purpose dependent adaptation of the mesh to smooth geometry. To define the boundary of a volume using NURBS, volumetric objects are defined by grouping curve-delimited surfaces together by a technique called boundary representation (BREP). This refers to a hierarchical, internally consistent tree structure of points (nodes), holes, and surfaces (loops), and surface enclosed pore volumes (body), recording their relations to each other (see for instance [54–57]). Third-order splines are used to represent grains and outer boundaries are resolved into surfaces with six side boundaries; four no-flow and two Dirichlet conditioned (inflow and outflow) boundaries (Fig. 7), for further import to the geometry editor of the mesh generation code.

E. Hybrid finite element mesh generation

An unstructured grid which can track free-form geometrical entities, such as NURBS, is then generated using hybrids of tetrahedral, hexahedral, prism, and pyramid elements (Fig. 8). This mesh is constructed with spatially variable adaptive refinement in order to honor the grain boundaries and also to capture the constricted pore regions. The use of prism, hexahedral, and pyramid elements with geometry-aligned high aspect ratio prevents a highly distorted mesh which could lead to large FE interpolation errors during flow simulations [58]. In all cases, only the pore space is meshed. The typical size of the mesh is in the range $1.4–1.8\times10^6$ elements (Table III) and the average size of the elements next to the grains is 0.9 μm. The average element size edge is 30 μm, compared to a mean grain diameter of around 500 μm. This resolution was chosen on the basis of previous sensitivity analysis [59] to secure mesh-independent results. An example of a typical three-dimensional (3D) mesh created in this work is shown in Fig. 8(A). Figure 8(B) corresponds to a 2D cut of the original 3D mesh illustrating the relative size of grains, pores, and elements.

F. Flow simulation

The creeping flow ($\mathrm{Re}\rightarrow0$) of an incompressible fluid is described by the Stokes equation and the continuity condition,

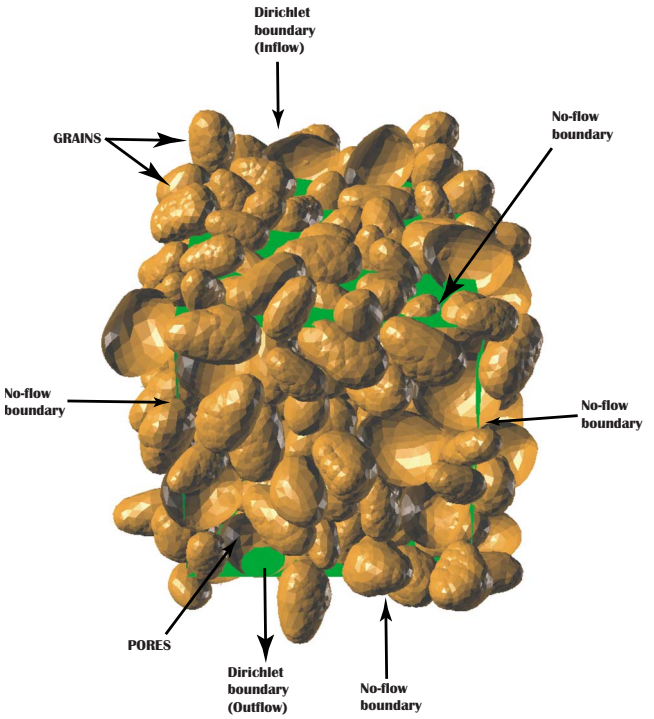

FIG. 7. (Color online) A CAD representation of the central core of the packs in Fig. 4 showing four no-flow and two Dirichlet (inflow and outflow) boundaries. Part of or whole grains that are not fully contained in the subvolume are discarded and only the pore space is meshed.

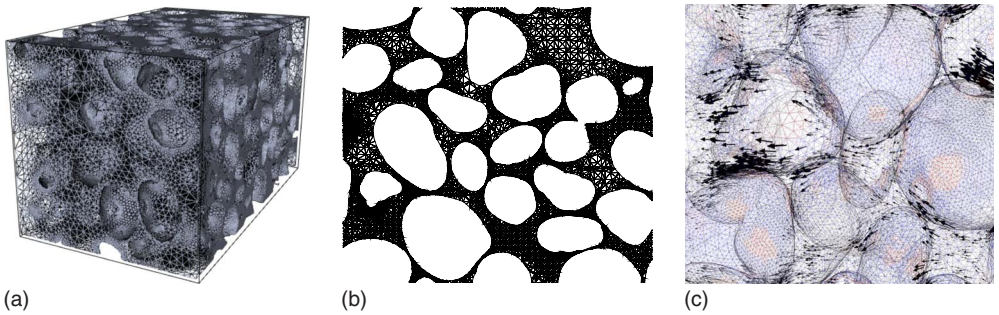

FIG. 8. (Color online) *A*: finite Element mesh of the CAD geometry shown in Fig. 7. *B*: 2*D* cut-plane of the mesh in *A*. *C*: flow field within a thin slice of the 3D pack as obtained in our simulations. Only a fraction of the vectors is shown for clarity.

$$\nu\nabla^2\vec{u} = \nabla P, \tag{7}$$

$$\nabla \cdot \vec{u} = 0, \tag{8}$$

where u, P, and ν are the velocity, pressure, and viscosity of the fluid, respectively. In the special case where the pressure gradient is aligned with the direction of flow, the Stokes equation reduces to the Reynolds lubrication equation. We solve the Stokes equation with this approximation using a two-step process detailed in [59]. The velocity is written as

$$\vec{u} = \frac{[\psi(x,y,z)]}{\nu} \nabla P, \tag{9}$$

where $\psi(x,y,z)$ represents a twice-differentiable real-valued function of the coordinates x, y, and z.

The function $\psi(x,y,z)$ obeys

$$\nabla^2\psi(x,y,z) = 1, \tag{10}$$

with $\psi(x,y,z)=0$ at the grain boundaries.

Substitution of Eq. (9) into Eq. (7) results in

$$\nabla^2(\psi(x,y,z)\,\nabla P) = \nabla P, \tag{11}$$

which can also be written as

$$\psi(x,y,z)\nabla^3 P + \nabla\psi(x,y,z)\nabla^2 P + \nabla^2\psi(x,y,z)\,\nabla P = \nabla P. \tag{12}$$

Neglecting the terms of order 3 in the pressure derivatives [first term in Eq. (12)] and substituting Eq. (10) in Eq. (12) gives

$$\nabla\psi(x,y,z)\nabla^2 P = 0, \tag{13}$$

which is solved for the pressure.

Having computed the velocity fields as described before, the permeability κ is computed thus

$$k = \frac{q\nu}{A\Delta P}, \tag{14}$$

where ΔP is the pressure difference per unit length along the direction of the main flow, ν is the viscosity, q is the volumetric flow, and A is the cross sectional area open to flow. Figure 8(C) shows the velocity field within a the 3D pack as obtained in our simulations.

TABLE III. Number of subsample sets from each of the models $A-E$ (Fig. 4), the range of porosity ϕ and number of finite elements used in the simulations.

Sample	No. of samples	ϕ range	No. of FE ($\times 10^6$)
A	5	0.33–0.38	1.6–1.8
B	5	0.32–0.37	1.4–1.8
C	5	0.33–0.38	1.6–1.8
D	7	0.36–0.38	1.6–1.7
E	5	0.34–0.39	1.4–1.8

III. RESULTS

A. Packing porosity

The porosity of the resulting packs depends on the particle shape and the friction coefficient used for the grain-grain interaction. When the intergranular friction is reduced, the packing density increases. This is particularly evident for the irregular shapes with a porosity variation in the range $33\% < \phi < 38\%$, (see Fig. 9). For the polydisperse spheres we obtained a narrow porosity range $35.2\% < \phi < 38.5\%$. The minimum porosity for the monosized spheres was ϕ_c

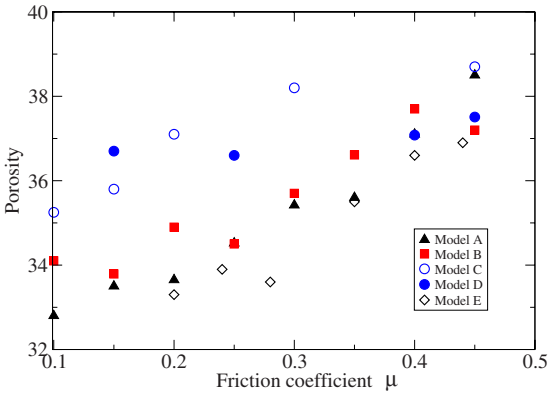

FIG. 9. (Color online) Porosities for varying friction coefficients μ for the models studied. Gaussian size distributions: semispherical particles model *A* (▲), elongated particles model *B* (■), spheres model *C* (○), monosize spheres model *D* (●), mixture of shapes binary size distribution model *E* (◇).

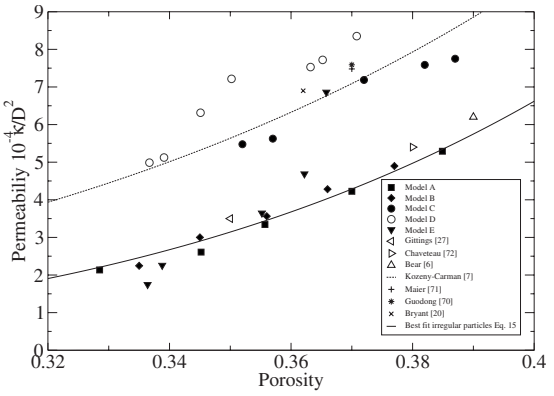

FIG. 10. Single phase permeability as function of porosity for samples of different heterogeneity and particle shape (see text).

≈36.6, similar to the porosity of a random close packing of monosized spheres reported previously [60,61]. The maximum porosity for the range of friction coefficients used was only marginally greater ϕ=37.3%. In order to compare later the permeability of the monosized spheres with the rest of the packs with smaller porosities, we produced a few extra packs by simulating the mechanical compaction of the monosized sphere pack following [62].

The dependency of the porosity on friction obtained here coincides with previous reported results for sphere packs [61,63]. Understandably, as the friction is reduced, more energy is available for grain rearrangement and the particles find their way to pack in denser configurations.

The relatively low ϕ of the packs of irregular particles in comparison with spheres apparently conflicts with some experiments [64,65] and simulations [8,66] where ϕ reduced as the sphericity was increased. On the contrary, for the same friction coefficient, sphere packs (ψ=1.0) are more porous than packs of irregular particles. Lower porosities than in sphere packs were also observed previously in packs of ellipsoids, rods, and cylinders [67–69], showing that when the particle shape deviates slightly from the perfect sphere, the packing density can improve.

The differences with some experiments is because we are modeling relatively smooth grains as found in some sands and not irregular fragments of crushed rocks/grains or rough particles. Roughness and angularity increase the effective friction and interlocking between grains and contribute to deteriorate the packing density.

B. Permeability

Figure 10 shows the computed permeabilities normalized by the squared harmonic mean diameter D^2 of the grains in each sample. The results reveal that the maximum difference in the permeability is by a factor of ≈2, when comparing samples with different particle shape and size distribution at nearly the same porosity.

The most permeable samples were the monosize sphere packs (set *D*). This is an expected result given the homogeneity of the sample and simplicity in the particle shape. This is a system extensively studied previously in the literature, so we can readily compare our results with available data. For instance, Bryant and Blunt [20] reported $\kappa/D^2=6.8\times10^{-4}$ using pore-networks for ϕ=36.2%. Guodong *et al.* [70] reported $\kappa/D^2=7.58\times10^{-4}$ and Maier *et al.* [71] obtained $\kappa/D^2=7.48\times10^{-4}$. In the latter two cases, ϕ=37% and κ was obtained using the Lattice-Boltzmann method. All these results are close to the empirical Kozeny-Carman correlation [7] also shown in the Fig. 10. In our simulations, the permeabilities are in the range of these results although we estimated slightly higher values. For ϕ=36.3% we computed $\kappa/D^2=7.46\times10^{-4}$ and $\kappa/D^2=8.24\times10^{-4}$ at ϕ=37%. In comparison with the monosized spheres, the packs of polydisperse spheres (set *C*) are slightly less permeable (see Fig. 10).

The effect of the particle shape can be addressed when comparing the sets *A*, *B*, and *C*. In these three sets, the size distribution is the same but in the sets *A* and *B* the particles are aspherical (see Sec. II B). The results in Fig. 10 show that the sphere packs are more permeable by a factor of around ≈1.6–1.8. The best fit of our data for irregular particles is

$$\frac{\kappa}{D^2}=0.11\phi^{5.6}, \tag{15}$$

which compares well with previous experimental results. For instance, Bear [6] reported a nondimensional permeability $\kappa/D^2=6.2\times10^{-4}$ for various sands of different heterogeneity with porosity range $\phi\approx$39%–40%. We obtain $\kappa/D^2=5.6\times10^{-4}$ at ϕ=39%. Chaveteau *et al.* [72] found $\kappa/D^2=5.4\times10^{-4}$ for packs of beads and some unconsolidated sands at $\phi\approx$38% while Gittings *et al.* [27] found $\kappa/D^2=3.5\times10^{-4}$ for relatively homogeneous sands in the range $\phi\approx$35%. In our case, $\kappa/D^2=4.9\times10^{-4}$ for ϕ=38% and $\kappa/D^2=3.1\times10^{-4}$ at porosity 35%. Clearly, the results obtained for these aspherical shapes were closer to these experimental values than in the case of simple spheres.

When comparing the sets of aspherical particles *A*,*B*,*E* alone, the particles in all the packs are different to the naked eye (see Fig. 4). However, the computed permeabilities in all the cases are similar with the only exception of one scattered point of sample *E* for which the permeability is closer to the spheres than to the rest of the packs.

Further insights can be gained by comparing our results with empirical correlations presented in the literature for different kinds of porous medium. In Fig. 11 the empirical fit proposed by Revil *et al.* [73] was obtained for shaly sands and might represent an extreme case of heterogeneity. The classical Kozeny-Carman equation is usually accepted to predict reasonably well the permeability of monosized sphere packs (see for instance [12,20,70]). Berg *et al.* [11], proposed a correlation for materials with different degrees of consolidation.

The Kozeny-Carman relation in its simplest form overpredicts the permeabilities in relation with the other experimental data in Fig. 11. This is in qualitative concordance with our simulation results. Indeed, our simulation results for aspherical particles lie close to the empirical fit proposed by Revil *et al.* [73]. Despite this, it is clear that the empirical and numerical fits in Fig. 11 do not differ substantially when compared at the same porosity. For instance, if we take a porosity

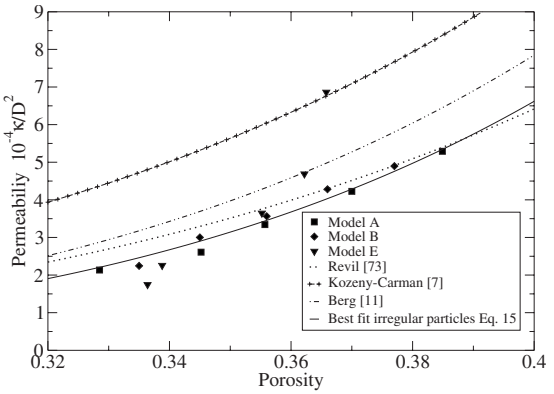

FIG. 11. Empirical correlations for different kinds of porous materials and in our numerical simulations.

ϕ=36% in the middle of the interval, the maximum difference is by a factor of about $\approx$3 despite the fact that each correlation is supposedly suited for a different kind of system (homogeneous spheres, consolidated, shaly unconsolidated). This indicates that the porosity is the key parameter controlling the permeability. Other parameters such as the grain size heterogeneity and particle shape contribute second-order corrections.

IV. CONCLUSIONS

We generated several granular packs polydisperse in particle shape and size by simulating the settling under gravity of the grains. The single-phase permeability was then compared within a range of porosities among packs of varying degrees of grain size heterogeneity and different particle shapes.

Our results indicate that the particle shape and size polydispersity have a small but noticeable effect on the hydraulic permeability. We found that sphere packs are between 1.6 to 1.8 times more permeable than packings of irregular grains. Yet, small differences in the shape of aspherical particles have little impact on the hydraulic conductivity, indicating that the porosity and the mean grain size are the most important parameters. We propose an empirical permeability-porosity relation for heterogeneous sand packs based on the data obtained in our simulations.

ACKNOWLEDGMENTS

We are grateful to Dr. Stefan Iglauer for providing the experimental data used in this study and to the pore-scale modeling group at Imperial College London for their cooperation. We also express our appreciations to the *PTDF* Nigeria and Rio Tinto for funding this work.

[1] M. A. Knackstedt and X. Zhang, Phys. Rev. E **50**, 2134 (1994).
[2] F. Dullien, *Porous Media: Transport and Microstructure*, 2nd ed. (Academic Press, New York, 1979).
[3] M. Sahimi, *Flow and Transport in Porous Media and Fractured Rock*, 2nd ed. (Weinheim, New York, 1995).
[4] S. Torquato, *Random Herogeneous Materials, Microstructure and Macroscopic Properties* (Springer, New York, 2002).
[5] C. H. Arns, M. A. Knackstedt, and N. S. Martys, Phys. Rev. E **72**, 046304 (2005).
[6] J. Bear, *Dynamics of Fluids in Porous Media* (Dover INC, New York, 1988).
[7] P. Carman, *Flow of Gases Through Porous Media* (Academic Press, New York, 1956).
[8] D. Coelho, J.-F. Thovert, and P. M. Adler, Phys. Rev. E **55**, 1959 (1997).
[9] F. D. Masch and K. J. Denny, Water Resour. Res. **2**, 655 (1966).
[10] W. Krumbein and G. Monk, Trans. Am. Inst., Min. Metall. Engineers **151**, 153 (1943).
[11] R. R. Berg, AAPG Bull. **59**, 939 (1975).
[12] E. Masad, B. Muhunthan, and N. Martys, Water Resour. Res. **36**, 851 (2000).
[13] J. G. Berryman and S. C. Blair, J. Appl. Phys. **60**, 1930 (1986).
[14] M. A. Ioannidis, M. J. Kwiecien, and I. Chatzis, J. Pet. Sci. Eng. **16**, 251 (1996).
[15] K. Witt, J. Geotech. Engrg. **109**, 1181 (1983).
[16] M. Stewart, A. Ward, and D. Rector, Adv. Water Resour. **29**, 1328 (2006).
[17] J. Koplik, C. Lin, and M. Vermette, J. Appl. Phys. **56**, 3127 (1984).
[18] E. C. Childs and N. Collis-George, Proc. R. Soc. London, Ser. A **201**, 392 (1950).
[19] S. L. Bryant, P. R. King, and D. W. Mellor, Transp. Porous Media **11**, 53 (1993).
[20] S. Bryant and M. Blunt, Phys. Rev. A **46**, 2004 (1992).
[21] P.-E. Øren and S. Bakke, Transp. Porous Media **46**, 311 (2002).
[22] L. M. Schwartz and J. R. Banavar, Phys. Rev. B **39**, 11965 (1989).
[23] M. Pilotti, Transp. Porous Media **33**, 257 (1998).
[24] P. Lehmann *et al.*, Adv. Water Resour. **31**, 1188 (2008).
[25] R. Hilfer and C. Manwart, Phys. Rev. E **64**, 021304 (2001).
[26] X. Garcia, J. P. Latham, X. Xiang, and J. Harrison, Geotechnique **59** (2009).
[27] P. Gittins *et al.*, AAPG Bull. (to be published).
[28] J. Santamarina and G. C. Cho, *Advances in Geotechnical Engineering: The Skempton Conference*, edited by R. J. Jardine, D. M. Potts, and K. G. Higgins (Thomas Telford , London, 2004).
[29] C. Lin and J. Miller, Powder Technol. **154**, 61 (2005).
[30] J. P. Latham, A. Munjiza, X. Garcia, J. Xiang, and R. Guises, Miner. Eng. **21**, 797 (2008).
[31] http://www3.imperial.ac.uk/earthscienceandengineering/research/energyenvmodmin /vgw
[32] sourceforge.net/projects/vgw/
[33] J. Ferellec and G. McDowell, Geomech. Geoeng. **3**, 211 (2008).
[34] L. Wang, J.-Y. Park, and Y. Fu, Constr. Build. Mater. **21**, 338

(2007).
[35] T. Matsushima and H. Saomoto, *Discrete Element Modeling for Irregularly-Shaped Sand Grains*, inProceedings of NUMGE2002: Numerical Methods in Geotechnical Engineering, edited by P. Mestat (LCPC, Paris, 2003), pp. 239-246.
[36] P. M. Hubbard, ACM Trans. Graphics **15**, 179 (1996).
[37] M. Price, V. Murariu, and G. Morrison, *Sphere Clump Generation and Trajectory Comparison for Real Particles*, in Proceedings of 5th International Conference on Discrete Element Methods, edited by P. Mestat (LCPC, Paris, 2007), pp. 239–246.
[38] G. C. Cho, J. Dodds, and J. C. Santamarina, J. Geotech. Geoenviron. Eng. **132**, 591 (2006).
[39] P. A. Cundall and O. D. L. Strack, Geotechnique **29**, 47 (1979).
[40] H. Zhu, Z. Zhou, R. Yang, and A. Yu, Chem. Eng. Sci. **63**, 5728 (2008).
[41] F. A. Tavarez and M. E. Plesha, Int. J. Numer. Methods Eng. **70**, 379 (2007).
[42] F. Fleissner, T. Gaugele, and P. Eberhard, Multibody Syst. Dyn. **18**, 81 (2007).
[43] J. Favier, M. M. H. Abbaspour-Fard, and A. R. Kremmer, Eng. Comput. **16**, 467 (1999).
[44] J. Shäfer, S. Dippel, and D. E. Wolf, J. Phys. I **6**, 5 (1996).
[45] A. E. H. Love, *Treatise on the Mathematical Theory of Elasticity*, 4th ed. (Dover INC, New York, 1944).
[46] L. E. Silbert, D. Ertas, G. S. Grest, T. C. Halsey, and D. Levine, Phys. Rev. E **65**, 031304 (2002).
[47] X. Garcia, M. Araujo, and E. Medina, Waves Random Media **14**, 129 (2004).
[48] W. Bosl, J. Dvorkin, and A. Nur, Geophys. Res. Lett. **25**, 1475 (1998).
[49] F. M. Auzerais *et al.*, Geophys. Res. Lett. **23**, 705 (1996).
[50] B. Ferrol and D. H. Rothman, Transp. Porous Media **20**, 3 (1995).
[51] L. M. Schwartz *et al.*, Physica A **207**, 28 (1994).
[52] P. Spanne, J. F. Thovert, C. J. Jacquin, W. B. Lindquist, K. W. Jones, and P. M. Adler, Phys. Rev. Lett. **73**, 2001 (1994).
[53] L. A. Piegl and W. Tiller, *The NURBS Book*, 2nd ed. (Springer-Verlag, Berlin, 1997).
[54] J. F. Thompson, B. Soni, and N. P. Weatherill, *Handbook of Grid Generation* (CRC Press, Boca Raton, FL, 1998).
[55] G. V. V. Ravi Kumar, Prabha Srinivasan, K. G. Shastry, and B. G. Prakash, Comput. Aided Des. **33**, 439 (2001).
[56] A. A. Mezentsev, A. Munjiza, and J.-P. Latham, *Unstructured Computational Meshes for Subdivision of Scanned Geological Objects*, in Proceedings of the 14th International Meshing Roundtable (Springer, New York, 2005) pp. 73–90,.
[57] M. Freytag and V. Shapiro, *B-rep SE: Simplicially Enhanced Boundary Representation*, in Proceedings of the 9th ACM Symposium on Solid Modeling and Applications, pp. 157–168 (Eurographics Association Genoa, Italy, 2004).
[58] A. Paluszny, S. K. Matthai, and M. Hohmeyer, Geofluids **7**, 186 (2007).
[59] L. T. Akanji and S. K. Matthai, Transp. Porous Media (to be published).
[60] S. Torquato, T. M. Truskett, and P. G. Debenedetti, Phys. Rev. Lett. **84**, 2064 (2000).
[61] L. E. Silbert, G. S. Grest, and J. W. Landry, Phys. Rev. E **66**, 061303 (2002).
[62] X. Garcia and E. Medina, Geophysics **71**, F13 (2006).
[63] Z. Zhang, L. Liu, Y. Yuan, and A. Yu, Powder Technol. **116**, 23 (2001).
[64] R. M. German, *Particle Packing Characteristics* (Metal Powder Industry, New Jersey, 1989).
[65] L. Rattan, *Encyclopedia of Soil Science* (CRC Press, Boca Raton, Fl, 2006).
[66] X. Jia, M. Gan, J. Williams, and D. Rhodes, Powder Technol. **174**, 10 (2007).
[67] A. Donev *et al.*, Science **303**, 990 (2004).
[68] S. R. Williams and A. P. Philipse, Phys. Rev. E **67**, 051301 (2003).
[69] M. Petrov *et al.*, Powder Metall. Met. Ceram. **43**, 330 (2004).
[70] J. Guodong, T. W. Patzek, and D. B. Silin, *Direct Prediction of the Absolute Permeability of Unconsolidated and Consolidated Reservoir Rock*, in Proceedings SPE Annual Technical Conference and Exhibition (SPE 90084) (Society of Petroleum Engineers Inc., Richardson, USA, 2004).
[71] R. S. Maier, D. M. Kroll, H. T. Davis, and R. S. Bernard, J. Colloid Interface Sci. **217**, 341 (1999).
[72] G. Chauveteau and A. Zaitoun, *Basic Rheological Behavior of Xanthan Polysaccharide Solutions in Porous Media: Effects of Pore Size and Polymer Concentration*, in Proceedings of the First European Symposium on Enhanced Oil Recovery (Elsevier, New York, 1981) p. 197212.
[73] A. Revil and L. I. Cathles, Water Resour. Res. **35**, 651 (1999).